The Astrophysical Journal, 931:132 (13pp), 2022 June 1 https://doi.org/10.3847/1538-4357/ac679d

Additional Evidence for a Pulsar Wind Nebula in the Heart of SN 1987A from Multiepoch X-Ray Data and MHD Modeling

Emanuele Greco[1,2,3,4], Marco Miceli[2,4], Salvatore Orlando[2], Barbara Olmi[2], Fabrizio Bocchino[2], Shigehiro Nagataki[5,6], Lei Sun[1,7], Jacco Vink[1,3], Vincenzo Sapienza[2,4], Masaomi Ono[5,6], Akira Dohi[6,8], and Giovanni Peres[2,4]
[1] Anton Pannekoek Institute for Astronomy, University of Amsterdam, Science Park 904, 1098 XH Amsterdam, The Netherlands; e.greco@uva.nl
[2] INAF-Osservatorio Astronomico di Palermo, Piazza del Parlamento 1, I-90134 Palermo, Italy
[3] GRAPPA, University of Amsterdam, Science Park 904, 1098 XH Amsterdam, The Netherlands
[4] Università degli Studi di Palermo, Dipartimento di Fisica e Chimica E. Segrè, Piazza del Parlamento 1, I-90134 Palermo, Italy
[5] Astrophysical Big Bang Laboratory (ABBL), RIKEN Cluster for Pioneering Research, 2-1 Hirosawa, Wako, Saitama 351-0198, Japan
[6] RIKEN Interdisciplinary Theoretical and Mathematical Sciences Program (iTHEMS), 2-1 Hirosawa, Wako, Saitama 351-0198, Japan
[7] Department of Astronomy, Nanjing University, Nanjing 210023, People's Republic of China
[8] Department of Physics, Kyushu University, 744 Motooka, Nishi-Ku, Fukuoka, Fukuoka 819-0395, Japan
Received 2022 March 15; revised 2022 April 13; accepted 2022 April 13; published 2022 June 2

Abstract

Since the day of its explosion, supernova (SN) 1987A has been closely monitored to study its evolution and to detect its central compact relic. In fact, the formation of a neutron star is strongly supported by the detection of neutrinos from the SN. However, besides the detection in the Atacama Large Millimeter/submillimeter Array (ALMA) data of a feature that is compatible with the emission arising from a protopulsar wind nebula (PWN), the only hint of the existence of such an elusive compact object is provided by the detection of hard emission in NuSTAR data up to ∼20 keV. We report on the simultaneous analysis of multiepoch observations of SN 1987A performed with Chandra, XMM-Newton, and NuSTAR. We also compare the observations with a state-of-the-art three-dimensional magnetohydrodynamic simulation of SN 1987A. A heavily absorbed power law, consistent with the emission from a PWN embedded in the heart of SN 1987A, is needed to properly describe the high-energy part of the observed spectra. The spectral parameters of the best-fit power law are in agreement with the previous estimate, and exclude diffusive shock acceleration as a possible mechanism responsible for the observed nonthermal emission. The information extracted from our analysis is used to infer the physical characteristics of the pulsar and the broadband emission from its nebula, in agreement with the ALMA data. Analysis of the synthetic spectra also shows that, in the near future, the main contribution to the Fe K emission line will originate in the outermost shocked ejecta of SN 1987A.

Unified Astronomy Thesaurus concepts: Supernova remnants (1667); Compact objects (288); Neutron stars (1108); Pulsars (1306); X-ray astronomy (1810); X-ray sources (1822); X-ray point sources (1270); Shocks (2086); Plasma astrophysics (1261); Interstellar synchrotron emission (856); X-ray observatories (1819); Magnetohydrodynamical simulations (1966)

1. Introduction

SN 1987A, located 51.4 kpc from Earth (Panagia 1999) in the Large Magellanic Cloud (LMC), was a core-collapse supernova (SN) discovered on 1987 February 23 (West et al. 1987). The dynamical evolution of the SN remnant (SNR) is strictly related to the highly inhomogeneous circumstellar medium (CSM), made of a dense and clumpy ring-like structure within a diffuse H II region (Sugerman et al. 2005). The evolution of SN 1987A has been extensively monitored at various wavelengths (McCray 1993; McCray & Fransson 2016): in particular, the X-ray band is ideal to investigate the interaction of the shock front with the CSM (e.g., Borkowski et al. 1997; Haberl et al. 2006; Park et al. 2006; Maggi et al. 2012; Maitra et al. 2022; Ravi et al. 2021; Sun et al. 2021) and the emission from the expected central compact relic of the SN explosion.

Despite the excellent understanding granted with deep and continuous observations and the detection of neutrinos from the SN (Bionta et al. 1987), which strongly indicate the formation of a neutron star (NS, Vissani 2015), a direct detection of the elusive compact object of SN 1987A is still missing. The most likely explanation for this nondetection is absorption by the innermost ejecta, i.e., the dense and cold material ejected by the SN and surrounding the putative compact object (Fransson & Chevalier 1987): because of the young age of SN 1987A, these ejecta are still very dense and the reverse shock generated in the outer shell of the SNR has not heated them yet. Photoelectric absorption from this metal-rich material can hide the X-ray emission from a compact leftover (Orlando et al. 2015; Alp et al. 2018; Esposito et al. 2018; Page et al. 2020).

The X-ray emission from a young NS may include a significant nonthermal component: the synchrotron radiation arising from its magnetosphere or from the pulsar wind nebula (PWN) associated with the rotating NS. Recently, Atacama Large Millimeter/submillimeter Array (ALMA) images showed a *blob* structure—located at the position where the compact object is expected to be—whose emission is compatible with the radio emission from a PWN (Cigan et al. 2019), though the same authors warned that the blob could be associated with other physical processes. Greco et al. (2021, hereafter G21) found indication of a PWN emitting in the hard X-ray band through the joint analysis of Chandra and NuSTAR

data collected in 2012 and 2014, though they cannot completely exclude that the nonthermal emission might be due to diffusive shock acceleration (DSA) at the shock front of the SNR. In contrast, Alp et al. (2021, hereafter A21) favor a thermal origin, with $kT \sim 4$ keV, for this hard emission from the analysis of XMM-Newton and NuSTAR data.

In this paper, we reanalyzed data from SN 1987A collected in 2012, 2014, and 2020 by Chandra, XMM-Newton, and NuSTAR with the aim of scrutinizing the hypothesis of a PWN deeply embedded in SN 1987A and understanding the origin of the different interpretations of the data discussed in G21 and A21. The analysis of the variability of the hard X-ray emission over 8 yr (a significantly longer time lapse than 2 yr, as in G21) can provide more conclusive indications on the nature of the source; for instance, it can help to discern between the DSA and PWN scenarios (see G21). Finally, in order to discriminate between the nonthermal and thermal origins of the emission above 10 keV as proposed by G21 and A21, respectively, we compared the observed spectra with those predicted by a state-of-the-art three-dimensional (3D) magneto-hydrodynamic (MHD) simulation of SN 1987A (model B18.3) described by Orlando et al. (2020, hereafter Or20). This allowed us to provide a coherent description of the multiepoch emission from 0.5 to 20 keV based on both standard data analysis and comparison of the data with the MHD simulation. In a companion paper (A. Dohi et al. 2022, in preparation), we investigate the detectability of the thermal emission counterpart from the putative central compact object (CCO) in SN 1987A.

The paper is organized as follows: in Section 2, we present the data and describe their analysis either adopting a traditional approach or using the MHD model B18.3, and we discuss the possible properties of the putative PWN, using available data as constraints for the spectrum; in Section 3, we discuss the results and their implications; in Section 4, we summarize the main findings and draw our conclusions; in the Appendix we investigate the detectability of the PWN in the soft X-ray band (0.5–8 keV).

2. X-Ray Data Analysis

We focused on the epochs when simultaneous (or almost simultaneous) Chandra, XMM-Newton, and NuSTAR observations of SN 1987A were performed. In particular, we analyzed data collected with Chandra/ACIS-S, XMM-Newton/pn, XMM-Newton/RGS, and NuSTAR/FPMA,B in 2012, 2014, and 2020. Details of the observations are reported in Table 1.

Spectral analysis has been performed with XSPEC (v12.11.1, Arnaud 1996) in the 0.5–8 keV, 0.3–10 keV, 0.35–2.5 keV, and 3–20 keV bands for the Chandra, XMM-Newton/pn, XMM-Newton/RGS, and NuSTAR data, respectively. We excluded from the analysis XMM-Newton/RGS bins with variance equal to 0 in order to avoid potential errors in the χ^2 estimate.

We reprocessed Chandra, XMM-Newton, and NuSTAR data with the standard pipelines available within CIAO v4.12.2, SAS v17.00.00, and NuSTARDAS v2.1.1, respectively. We extracted Chandra and NuSTAR spectra following G21, and the XMM-Newton spectra following Sun et al. (2021, hereafter S21). All the spectra are rebinned optimally following the procedure described by Kaastra & Bleeker (2016), and the background spectrum for subtraction was extracted from a nearby region immediately outside the source (see G21). We verified that our results are not affected by the choice of the background regions.

Table 1
Summary of the Main Characteristics of the Analyzed Observations

Telescope	Obs. ID	PI	Date (year/month/day)	Exposure Time (ks)
Chandra	3830	Burrows	2003/07/08	45
	13735	Burrows	2012/03/28	48
	14417	Burrows	2012/04/01	27
	15809	Burrows	2014/03/19	70
	15810	Burrows	2014/09/20	48
	22425	Burrows	2020/09/12	61
	24652	Burrows	2020/09/17	29
NuSTAR	40001014003	Harrison	2012/09/08	136
	40001014004	Harrison	2012/09/11	200
	40001014007	Harrison	2012/10/21	200
	40001014018	Harrison	2014/06/15	200
	40001014020	Harrison	2014/06/19	275
	40001014023	Harrison	2014/08/01	428
	40501004002	Alp	2020/05/13	183
	40501004004	Alp	2020/05/27	159
XMM-Newton	0690510101	Haberl	2012/12/11	70/53[a]
	0743790101	Haberl	2014/11/29	81/50[a]
	0862920201	Haberl	2020/11/24	81/50[a]

Note.
[a] XMM-Newton/pn unfiltered/filtered exposure time.

2.1. Standard Analysis of the Spectra

We considered three clusters of observations, one for each epoch, namely 2012, 2014, and 2020. We simultaneously analyzed Chandra, XMM-Newton, and NuSTAR spectra for each selected year by adopting a model composed of a foreground absorption component (`TBabs` model in XSPEC; Arnaud 1996), and components of optically thin isothermal plasma in nonequilibrium of ionization (`vnei` model). We included a multiplicative factor C_i, which takes into account cross-calibration between different detectors (the index i running through the various instruments). For the XMM-Newton/RGS spectra, a `gsmooth` component and a `vashift` component are also included, with values fixed to those of S21, to account for line broadening and line shift due to the systemic motion of SN 1987A, respectively. The foreground column density $N_{\rm H}$ is fixed to 2.35×10^{21} cm^{-2} (Park et al. 2006). In the following, we refer to this model as the $2kT$ model or $3kT$ model, depending on the number of `vnei` components included. We found the cross-calibration factors to differ from 1 by <5% between Chandra and XMM-Newton spectra and by <10% between NuSTAR and XMM-Newton (and between NuSTAR and Chandra), compatible with the characteristic values (Madsen et al. 2015).

Temperature, emission measure, ionization parameter, and abundances of O, Ne, Mg, Si, S, and Fe were left free to vary in the fitting process and the other abundances were kept fixed to typical values for the LMC (Russell & Dopita 1992).

Before fitting simultaneously the spectra collected by all telescopes, we analyzed the Chandra and XMM-Newton

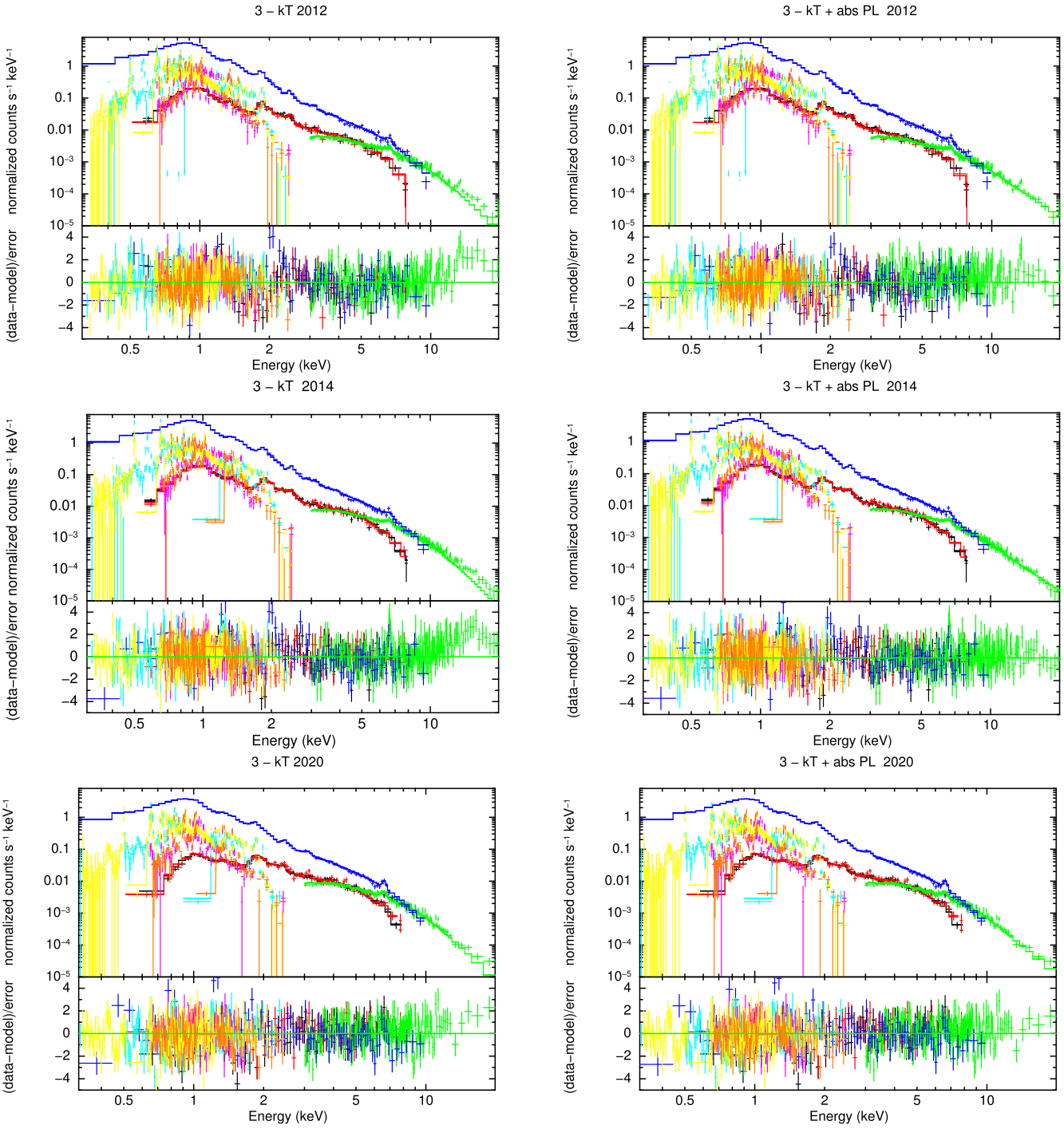

Figure 1. Chandra/ACIS-S, XMM-Newton/pn,RGS, and NuSTAR/FPMA,B spectra of SN 1987A in 2012 (first row), 2014 (second row), and 2020 (third row) with the corresponding residuals. NuSTAR spectra are summed for visualization purposes only. Different colors identify different spectra: Chandra in black and red; NuSTAR in green; XMM-Newton/PN in blue; XMM-Newton/RGS in yellow, cyan, orange, and light green. The spectra are simultaneously fitted either with the 3kT model (left panels) or with the 3kT model plus an absorbed PL (right panels), representing the PWN scenario.

spectra separately. We reproduced the same results as G21 for the 2012 and 2014 Chandra data and the same as S21 for the multiepoch XMM-Newton data. In particular, both Chandra and XMM-Newton data can be well reproduced by considering the 2kT model. Including a third thermal component does not improve the fit quality of the Chandra spectra, while it leads to a significantly better description of the XMM-Newton data due to the higher statistics of the data and sensitivity of the XMM-Newton detectors. Thus, we fitted the 0.5–20 keV spectra jointly collected by Chandra, XMM-Newton, and NuSTAR with the 3kT model, since it provides the best description in this case. The spectra, with the corresponding best-fit 3kT model for each epoch, are shown in the left panels of Figure 1. The best-fit parameters are shown in Table 2.

The resulting 3kT best-fit model provides an acceptable description of the data in the 0.3–10 keV band in all epochs,

Table 2
Best-fit Parameters of the 3*kT* Model and the 3*kT* Plus Absorbed PL Model

Component	Parameter	3*kT* Model			3*kT* + Absorbed PL Model		
		2012	2014	2020	2012	2014	2020
TBabs	$N_{\rm H}$ (10^{22} cm^{-2})	0.235 (fixed)					
vnei$_1$	kT_1 (keV)	$0.42^{+0.04}_{-0.03}$	$0.41^{+0.03}_{-0.02}$	0.48±0.06	0.40±0.03	0.40±0.03	$0.48^{+0.05}_{-0.07}$
	O	$0.158^{+0.015}_{-0.008}$	$0.19^{+0.01}_{-0.02}$	$0.16^{+0.03}_{-0.01}$	$0.169^{+0.012}_{-0.013}$	$0.196^{+0.017}_{-0.016}$	$0.16^{+0.03}_{-0.02}$
	Ne	$0.42^{+0.04}_{-0.02}$	0.50±0.04	$0.38^{+0.02}_{-0.04}$	$0.46^{+0.04}_{-0.02}$	$0.54^{+0.08}_{-0.03}$	0.38±0.5
	Mg	$0.56^{+0.06}_{-0.04}$	$0.62^{+0.03}_{-0.06}$	$0.49^{+0.04}_{-0.02}$	$0.59^{+0.02}_{-0.04}$	0.64±0.4	$0.50^{+0.03}_{-0.04}$
	Si	$0.82^{+0.05}_{-0.04}$	0.84±0.4	0.71±0.04	$0.83^{+0.04}_{-0.05}$	0.84±0.04	$0.71^{+0.05}_{-0.04}$
	S	$0.67^{+0.07}_{-0.08}$	$0.72^{+0.06}_{-0.07}$	$0.57^{+0.06}_{-0.07}$	0.64±0.07	$0.69^{+0.07}_{-0.06}$	0.57±0.06
	Fe	$0.368^{+0.023}_{-0.016}$	$0.396^{+0.018}_{-0.017}$	$0.337^{+0.020}_{-0.011}$	$0.398^{+0.016}_{-0.020}$	0.42±0.02	$0.342^{+0.022}_{-0.011}$
	τ_1 (10^{11} s cm^{-3})	$1.02^{+0.17}_{-0.06}$	0.77±0.13	$0.77^{+0.20}_{-0.05}$	$1.04^{+0.15}_{-0.11}$	$0.78^{+0.20}_{-0.11}$	$0.79^{+0.15}_{-0.12}$
	EM$_1$ (10^{58} cm^{-3})	$13.7^{+1.0}_{-1.1}$	8.3 ± 1.0	5.9±0.9	$12.8^{+0.9}_{-1.1}$	8.3±0.8	$5.9^{+0.8}_{-0.8}$
vnei$_2$	kT_2 (keV)	$0.87^{+0.05}_{-0.03}$	$0.83^{+0.01}_{-0.02}$	$0.96^{+0.06}_{-0.05}$	$0.84^{+0.02}_{-0.03}$	$0.827^{+0.012}_{-0.020}$	$0.96^{+0.03}_{-0.05}$
	τ_2 (10^{11} s cm^{-3})	$1.83^{+0.19}_{-0.17}$	$2.11^{+0.24}_{-0.12}$	$1.4^{+0.3}_{-0.2}$	$1.7^{+0.4}_{-0.2}$	$1.9^{+0.3}_{-0.2}$	$1.41^{+0.25}_{-0.10}$
	EM$_2$ (10^{58} cm^{-3})	$16.3^{+0.9}_{-0.6}$	$17.3^{+0.6}_{-1.1}$	$11.8^{+0.9}_{-1.0}$	$15.1^{+0.9}_{-1.0}$	$15.8^{+0.9}_{-0.4}$	$11.6^{+0.5}_{-0.6}$
vnei$_3$	kT_3 (keV)	3.54±0.07	$3.36^{+0.12}_{-0.05}$	$3.34^{+0.08}_{-0.07}$	$2.91^{+0.07}_{-0.10}$	$2.87^{+0.04}_{-0.14}$	$3.18^{+0.012}_{-0.20}$
	τ_3 (10^{11} s cm^{-3})	$0.89^{+0.08}_{-0.05}$	1.01±0.5	$1.13^{+0.10}_{-0.09}$	$1.09^{+0.14}_{-0.1}$	$1.28^{+0.12}_{-0.11}$	$1.21^{+0.15}_{-0.13}$
	EM$_3$ (10^{58} cm^{-3})	$5.51^{+0.11}_{-0.08}$	$6.86^{+0.09}_{-0.18}$	$9.2^{+0.4}_{-0.3}$	$6.8^{+0.5}_{-0.2}$	8.0±0.3	$9.5^{+0.5}_{-0.4}$
power-law[a]	Γ	...	...	...	$3.0^{+0.4}_{-0.2}$	$2.9^{+0.3}_{-0.4}$	$2.6^{+0.7}_{-1.8}$ [b]
	norm (10^{-4} ph s^{-1} keV^{-1} cm^{-2})	...	...	...	15^{+25}_{-5}	10^{+14}_{-9}	2^{+9}_{-1} [b]
	Flux$_{0.5-8}$ (10^{-13} erg s^{-1} cm^{-2})	96.1±0.05	$98.3^{+0.5}_{-0.4}$	$91.3^{+0.5}_{-0.6}$	96.1±0.05	$98.3^{+0.5}_{-0.4}$	$91.3^{+0.5}_{-0.6}$
	Flux$_{10-20}$ (10^{-13} erg s^{-1} cm^{-2})	1.19±0.09	1.28±0.06	$1.52^{+0.13}_{-0.14}$	$1.51^{+0.13}_{-0.11}$	$1.59^{+0.09}_{-0.08}$	$1.76^{+0.15}_{-0.17}$
	χ^2/d.o.f.	2754/2139	2912/2199	2382/1897	2680/2137	2814/2197	2377/1895
	$\chi^2_{\rm red}$	1.29	1.32	1.26	1.25	1.28	1.25
		MHD model			MHD + absorbed PL model		
	χ^2/d.o.f. (RGS1 first order)	893/457	959/456	1677/434	...	...	...
	χ^2/d.o.f. (pn, ACIS-S, FPMA,B)	1375/553	1547/588	1933/459	864/551	694/586	1643/457

Notes. Abundance values are expressed with respect to Wilms et al. (2000). Abundances of other elements are kept fixed to those found by Russell & Dopita (1992). Uncertainties are estimated at 90% confidence level, unless otherwise stated.
[a] The power-law is coupled to the vphabs component built from the MHD model.
[b] Uncertainties estimated at 68% confidence level.

even though clear residuals systematically show up at energies above 10 keV. Our best-fit values of temperatures are consistent at a 90% confidence level with the results of A21.

We also reproduced the results of A21, based on a model with three vpshock components, and we noticed that the observed excess in the 10–20 keV band is not significant when adopting this model. However, the measured values of the ionization ages are much higher than expected for SN 1987A, as also noted by A21 (see also S21 and Ravi et al. 2021). In light of this, we discuss the results based on the vnei model, which indicates that all the plasma components are under-ionized, as also reported by, e.g., Zhekov et al. (2009), Park et al. (2006), Miceli et al. (2019), Ravi et al. (2021), and S21.

As a next step, following G21, we investigated whether a power-law (PL) component, heavily absorbed by the inner cold ejecta ($T_{\rm ej} \sim 10$ K), added to the 3*kT* model significantly improves the fit. The PL component is associated with the nonthermal emission arising from a PWN embedded in the center of SN 1987A.

The absorption of cold ejecta was calculated from model B18.3 (Or20) by adopting the same approach as in G21: we used the XSPEC photoelectric absorption model vphabs and the distributions of temperature, density, and abundance derived in the whole spatial domain in model B18.3 to properly calculate, for each epoch, the absorption by the ejecta for a source located where model B18.3 predicts the NS is, considering a kick velocity of 500 km s^{-1}.[9] We verified that our results do not change significantly if we consider kick velocities between 300 and 700 km s^{-1}. We estimated that the corresponding column density $N_{\rm H}$ is $\gtrsim 10^{23}$ cm^{-2}, two orders of magnitude higher than the foreground absorption.

Including the additional absorption component due to the innermost ejecta is important to properly understand the physical origin of a putative nonthermal component: the emission stemming from the PWN is absorbed by this cloud of cold ejecta, leading to a negligible emission contribution at energies $\lesssim$5 keV (see G21 and also the Appendix). Indeed, we found that the additional absorbed PL component significantly improves the fit of the spectra at all epochs. We verified that this additional component is statistically needed: its normalization is higher than 0 at the 5σ confidence level in 2012 and

[9] The absorption models for all the epochs have been made available in a public repository, as well the spectra and the best-fit models discussed in the whole paper, at the link doi:10.5281/zenodo.6591454.

Table 3
Best-fit Parameters of the Multiepoch 3*kT* Plus Absorbed PL Model

Component	Parameter	2012	2014	2020
TBabs	$N_{\rm H}$ (10^{22} cm^{-2})		0.235 (fixed)	
vnei$_1$	kT_1 (keV)	0.40±0.02	$0.42^{+0.03}_{-0.04}$	$0.47^{+0.04}_{-0.06}$
	O		$0.176^{+0.006}_{-0.005}$	
	Ne		$0.47^{+0.03}_{-0.02}$	
	Mg		0.59±0.02	
	Si		$0.80^{+0.03}_{-0.02}$	
	S		$0.64^{+0.04}_{-0.04}$	
	Fe		$0.391^{+0.007}_{-0.008}$	
	τ_1 (10^{11} s cm^{-3})	$1.03^{+0.19}_{-0.10}$	0.80±0.11	$0.766^{+0.017}_{-0.010}$
	EM$_1$ (10^{58} cm^{-3})	$12.5^{+0.7}_{-0.5}$	$8.8^{+0.4}_{-0.9}$	$5.7^{+0.4}_{-0.5}$
vnei$_2$	kT_2 (keV)	$0.827^{+0.010}_{-0.019}$	$0.828^{+0.008}_{-0.007}$	$0.98^{+0.03}_{-0.02}$
	τ_2 (10^{11} s cm^{-3})	1.89±0.17	$1.83^{+0.15}_{-0.13}$	$1.47^{+0.10}_{-0.17}$
	EM$_2$ (10^{58} cm^{-3})	$15.8^{+0.2}_{-0.7}$	$16.5^{+0.5}_{-0.4}$	10.4±0.3
vnei$_3$	kT_3 (keV)	2.96±0.06	$2.92^{+0.07}_{-0.05}$	$2.90^{+0.07}_{-0.03}$
	τ_1 (10^{11} s cm^{-3})	$1.05^{+0.08}_{-0.05}$	$1.17^{+0.06}_{-0.08}$	$1.60^{+0.08}_{-0.11}$
	EM$_3$ (10^{58} cm^{-3})	6.7±0.2	7.8±0.2	$10.1^{+0.3}_{-0.2}$
power-law[a]	Γ		2.8 (fixed)	
	norm (10^{-4} photons s^{-1} keV^{-1} cm^{-2})		$7.1^{+0.6}_{-0.9}$	
	$L^{\rm PWN}_{10-20}$ (10^{34} erg s^{-1})		3.0±0.3	
	χ^2 (d.o.f.)		7831 (6162)	

Notes. Abundance values expressed with respect to Wilms et al. (2000) and assumed constant between the three epochs. Abundance of other elements are kept fixed to those found by Russell & Dopita (1992). Uncertainties are estimated at 90% confidence level.
[a] The power law is coupled to the vphabs component built from the MHD model.

2014, and at the 2σ confidence level in 2020. The improved χ^2 values obtained when including the absorbed PL are $\Delta\chi^2_{2012} = -74$, $\Delta\chi^2_{2014} = -98$, and $\Delta\chi^2_{2020} = -5$ with respect to the 3*kT* scenario alone. The spectra fitted with this 3*kT* plus absorbed PL model and the corresponding residuals are shown in the right panels of Figure 1. The best-fit parameters are reported in Table 2.

By looking at the residuals in Figure 1, we see that the 3*kT* and 3*kT* plus absorbed PL models provide a very similar description of the spectra in the 0.3–10 keV energy band, but residuals between 10 and 20 keV show up when the absorbed PL component is not included, indicating that the purely thermal model is not the best suited for these data points. By adding the absorbed PL, these points are satisfyingly reproduced.

The PL parameters are better constrained by 2014 data, thanks to the higher statistics available and the smaller error bars, with the photon index Γ in the range [2.5–3.2]. For each year considered, Γ and the normalization of the PL are consistent with being constant, and so also is the flux in the 10–20 keV band. We checked that no significant changes in the description of the spectra are observed by fixing the photon index to 2.8 (the average of the best-fit values derived through the epochs), with a variation $\Delta\chi^2 \lesssim 2$ points.

We also noticed a decrease in the best-fit flux of the power law for the 2020 data. However, we found no significant worsening of the fit quality when imposing the 2014 PL component to fit the 2020 data set: we argue that the observed decrease in the flux derived for the 2020 data is not due to an intrinsic decrease in the nonthermal emission but rather reflects the increase in the contribution from thermal emission in this band. The less relevant contribution of the PL component to the total X-ray spectrum in 2020 (while this relative contribution is significant in 2012 and 2014) is consistent with the scenario of nonthermal emission originating from a PWN: since we expect no significant variations of the PWN luminosity over a time lapse of a decade (Torres et al. 2014), the constant contribution of the PL component to the spectrum is gradually overwhelmed by the increasing contribution of the thermal emission. We will further discuss this aspect in Sections 2.2 and 3.

To further investigate this aspect, we performed a multiepoch simultaneous fit of all the data considered in this work, analogously to that done by G21. We simultaneously fit the 2012, 2014, and 2020 data with a 3-vnei plus absorbed PL model with the normalization, electron temperature, and ionization ages of the vnei components free to vary, while the abundance values are free to vary but forced to be constant in time.

Coherently with what has been discussed above, we also fixed the photon index $\Gamma = 2.8$, leaving only the PL normalization free to vary. We found a very significant improvement in the fit when including the absorbed PL in the model: from $\chi^2_{\rm thermal} = 7997$ (6163 dof) to $\chi^2_{\rm PWN} = 7831$ (6162 dof). Best-fit parameters of the simultaneous multiepoch analysis are shown in Table 3.[10]

These confirm that the spectral characteristics of the absorbed PL found in this work are consistent with the findings by G21 and that the intrinsic PWN luminosity in the 10–20 keV band is constant over the three epochs at a value

[10] The best-fit parameters of the 3*kT* model are not shown since these are just the same as those found with the single-year analysis.

of $\sim 3 \times 10^{34}$ erg s^{-1}. This is also in agreement with the almost constant X-ray flux in the [10–24] keV band reported by A21.

G21 noted that the nonthermal emission revealed in the hard X-ray spectra of SN 1987A could also be due to DSA at the SNR shock front, and that it is not possible to discern between DSA and PWN scenarios with 2012 and 2014 data alone. Thanks to the data collected in 2020, we can now verify which of the two scenarios best describes the multiepoch spectra. To this end, we considered the case in which the nonthermal emission originates from DSA occurring in the outer shells of SN 1987A. Thus, we fitted the 2012, 2014, and 2020 data with a $3kT$ plus PL model, i.e., without considering absorption from the ejecta, since now the source is not embedded in the cold and dense innermost ejecta but is close to the remnant border. The best-fit value of Γ is ~ 2, compatible with the canonical photon index for synchrotron radiation. However, we found χ^2 values worse than those obtained in the $3kT$ plus absorbed PL scenario, with $\Delta\chi^2_{2012} = 15$, $\Delta\chi^2_{2014} = 15$, and $\Delta\chi^2_{2020} = 2$, with the same degrees of freedom. We further discuss this scenario in Section 3.

2.2. Interpretation of the Data with the MHD Model

The analysis of Chandra, XMM-Newton, and NuSTAR data from SN 1987A discussed in the previous section points toward a detectable nonthermal component, strongly absorbed and distinctly contributing to the hard X-rays. On the other hand, results from A21 based on 3-`vpshock` model point toward a thermal origin of this emission, though the ionization ages of the three components are not compatible with those expected for SN 1987A (e.g., Park et al. 2006; Zhekov et al. 2009; Miceli et al. 2019; Ravi et al. 2021; S21). To further investigate this issue, we took a step beyond the standard fits of X-ray spectra with a few phenomenological spectral components, and used the 3D MHD model B18.3 by Or20 to investigate the thermal contribution of the shock-heated plasma to the X-ray spectra of SN 1987A.

The advantage of this approach is to describe the multiepoch thermal X-ray emission from SN 1987A with a single *physical* model that follows self-consistently the evolution of the SNR since the SN event, providing an almost continuous distribution of plasma temperatures, ionization parameters, and emission measures at all epochs. Model B18.3 has been well constrained by multiwavelength observations of the progenitor star, the parent SN, and the SNR. It considers a stellar model that describes the main characteristics of the progenitor star of SN 1987A (Urushibata et al. 2018) and reproduces the main properties of the anisotropic SN explosion (Ono et al. 2020) and the thermal X-ray emission from the SNR in the 0.5–10 keV band (Or20).

Model B18.3 does not include a description of a hypothetical PWN. Thus, from the model, we only synthesized the thermal X-ray emission from the shock-heated plasma, assuming the abundances found by S21 and considering the effects of thermal and Doppler broadening of emission lines (derived from the distributions of ion temperatures and plasma velocities along the line of sight from model B18.3) in the synthesis of the spectra (see Miceli et al. 2019). The plasma temperature, the ionization parameter, and the emission measure are provided by model B18.3 at all epochs in a self-consistent fashion.

A few (<10) numerical cells of the model, comprising cold ($T < 10^6$ K) and dense ($n > 7.5 \times 10^4$ cm^{-3}) plasma (which contributes mainly to the very soft X-ray emission below 1 keV, which is not the focus of this work), were rejected from the analysis. In fact these cells correspond to dense clumps of plasma subject to a strong radiative cooling with a size comparable to (or smaller than) that of the cells. As a result, these clumps are not well described by the adopted spatial resolution.

We did not perform any fit on the model parameters,[11] but we just compared the spectra as they are synthesized from model B18.3 with the actual ones at all epochs and without any renormalization of the model or ad hoc assumptions. In comparing synthetic and actual spectra, we only left the factors C_i free to vary, to account for cross-calibration issues. As done in the standard analysis, we put $C_{\rm pn} = 1$ (for the XMM-Newton/pn spectra) and all other C_i were forced to stay within their typical ranges (Madsen et al. 2015). The comparison between the thermal emission predicted by model B18.3 and the actual data for each epoch is shown in the first row of Figure 2 for the XMM-Newton/RGS1 (first order) and in the second row for XMM-Newton/pn, Chandra/ACIS-S, and NuSTAR/FPMA.

We stress that the plots in Figure 2 were obtained without performing any fit, except for the cross-calibration constants. It is striking that the model is able to reproduce well the X-ray emission below 10 keV at all epochs and for all instruments, even the main lines and the continuum emission observed by RGS1. This strongly suggests that model B18.3 accurately describes the thermal contribution to X-rays from the shock-heated plasma and its evolution in the time lapse considered.

The good description of the line widths that we see in the first row of Figure 2 also indicates that the spatial distribution of macroscopic plasma velocity (mainly responsible for the line broadening) is also well reproduced by model B18.3, further confirming the pertinence of this model. Model B18.3 only slightly overestimates the flux in the 2020 data, as also shown by the X-ray light curves in Or20.

Furthermore, Figure 2 shows that model B18.3 self-consistently describes the rapid evolution of thermal emission in the 0.5–8 keV band in the 2012–2020 time range. In particular, it accounts for the increase in the emission measure of the hot plasma associated with the expansion of the shock in the H II region and with the hardening of X-ray spectra reported by Frank et al. (2016), S21, and Ravi et al. (2021). However, we also note that the thermal emission synthesized from model B18.3 underestimates the X-ray flux above ~ 8 keV. Interestingly, the difference between synthetic thermal emission and actual X-ray spectra above 8 keV does not evolve, but stays constant between 2012 and 2014. This indicates that an additional steady, hard X-ray-emitting component needs to be included.

Since this model already takes into account all possible contributions from thermal shock-heated plasma and self-consistently describes their temporal evolution, in the light of the results of Section 2.1, it is natural to assert that the radiation in the hard-energy part of the X-ray spectra most likely includes a steady nonthermal component. This strongly corroborates the result of our spectral analysis, which showed that a nonthermal component is needed to achieve the best description of the data.

[11] We only associate a systematic error of 5% on the synthetic spectra when comparing them to the XMM-Newton/pn data because of the very small error bars on the data set collected by this detector.

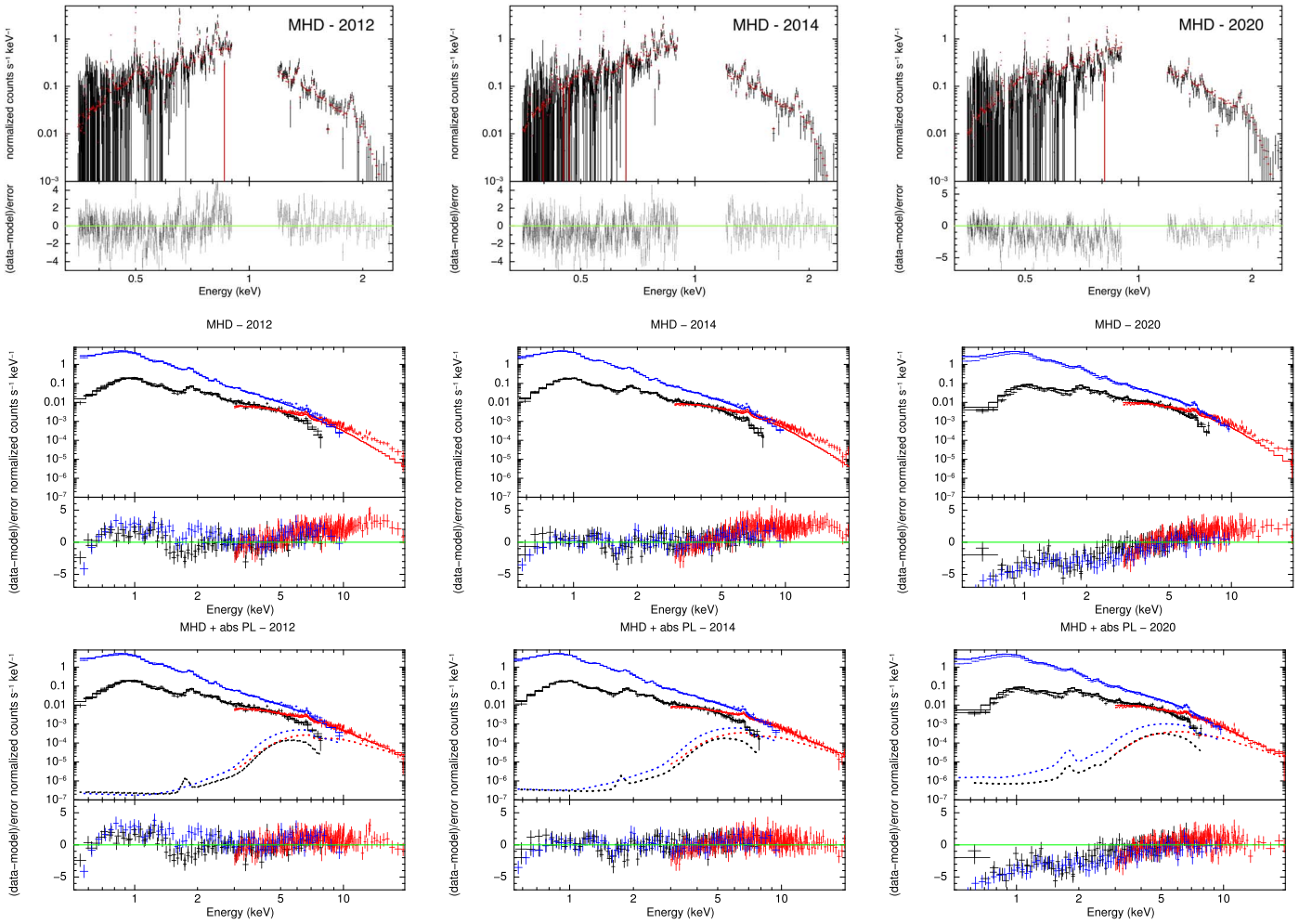

Figure 2. Same as Figure 1 but XMM-Newton/RGS1 spectra are shown separately in the first row. Black, blue, and red points are Chandra/ACIS-S, XMM-Newton/pn, and NuSTAR/FPMA,B spectra, respectively. First and second rows: the spectra are compared with the MHD model by Or20 (solid lines). Last row: the spectra are compared with the MHD model by Or20 plus the PWN component found in this paper (solid lines). The contribution of the absorbed PL folded with each response matrix is also shown with dashed lines of the same color as the corresponding data points.

As a further step, we compared the actual spectra with the thermal emission synthesized from model B18.3 plus the absorbed PL component inferred from the spectral analysis in the previous section (and consistent with that found by G21), representing the emission from the PWN. To this end, we assumed the same PL parameters as those found in the simultaneous multiepoch fit, namely those that are best constrained: $\Gamma = 2.8$ and norm $= 7.1 \times 10^{-4}$ photons s^{-1}keV^{-1} cm^{-2}. We verified that, by changing the norm value in the range $[4\text{–}8] \times 10^{-4}$ photons s^{-1} keV^{-1} cm^{-2} the results do not significantly change. Coherently with the standard analysis, the foreground absorption component is kept fixed at 2.35×10^{21} cm^{-2} (Park et al. 2006). Again, we did not perform any fit to fine-tune the photon index and the normalization of the PL. The third row in Figure 2 compares the synthetic spectra derived from model B18.3 plus the absorbed PL with the actual spectra at the three epochs. In the bottom rows of Table 2, we report the values of χ^2 obtained when comparing the actual data with the emission synthesized either from model B18.3 alone or from model B18.3 plus the absorbed PL.

Analogously to what we found with the standard analysis, an additional component described by a steady and heavily absorbed PL is needed for the best description of the actual data. This is a further indication of the nonthermal nature of the dominant emitting component above 10 keV and of heavy absorption of this component compatible with being embedded in the innermost ejecta.

2.3. A Deeper Look into the Putative PWN

In this section we make use of available spectral information to get a closer look into the elusive PWN and pulsar possibly hidden inside SN 1987A, with the main purpose of determining a range for the pulsar spin-down luminosity, $\dot{E}$, and period, P, to be compared with those of other known objects.

We built a simple model for the PWN synchrotron spectrum considering, as is generally done, a broken power law with energy flux given by $S_\nu(\nu) \propto \nu^{-\alpha_1}$ for $\nu \leqslant \nu_B$ and $S_\nu(\nu) \propto \nu^{-\alpha_2}$ otherwise, with a main spectral break at a frequency ν_B (see, e.g., Gaensler & Slane 2006; Slane 2017, for a review on PWN properties). PWNe have been shown to be characterized by a rather flat radio spectrum at all frequencies below ν_B, with an energy spectral index in the range $\alpha_1 \simeq 0\text{–}0.4$ (see, e.g., Reynolds et al. 2017). On the other hand, the emission at higher energies is well described by a steeper PL, with a photon index in the X-ray band of $\Gamma_2 \approx 2.2$ (with $\Gamma = 1 + \alpha$). Apart from the spectral break separating the two populations of particles responsible for the low- and high-energy emissions,

a number of other spectral variations are observed from optical to gamma-ray bands, with some evidence for a spectral steepening with increasing distance from the PWN center in X-rays (see Reynolds et al. 2017, and references therein).

For the present work we have assumed $\alpha_1 = 0.3$ for the low-energy spectral component. However, we verified that considering a lower value causes a negligible variation to the final estimate of the pulsar spin-down luminosity and period. The analysis of the X-ray spectra, as discussed above in this section (see Section 2.1 and Table 2 therein), gave us an indication of the nonthermal photon index in the hard X-ray band ($\Gamma = 2.8$ at 10–20 keV). Despite being slightly higher than the one usually found for X-ray spectra of PWNe, it is still compatible with previous observations: (i) if confirmed, the PWN of SN 1987A would be the youngest ever found, likely characterized by higher magnetic field than other objects (Torres et al. 2014); (ii) the typical X-ray Γ is usually measured in the 0.5–8 keV band, while here we are able to measure only the very hard part of the spectrum, whose slope might be modified by the proximity of the synchrotron cutoff. The frequency of the spectral break is indeed left as a free parameter of the model.

The only other available observational information on the properties of the putative PWN comes from ALMA's measurements of a radio blob (of radius 0.01 pc), detected at 679 GHz with a flux of 1–2 mJy, interpreted as the result of an equivalent bolometric luminosity in the range $L_R = 40$–$90\ L_\odot$ and located at the position where the pulsar supposedly formed (Cigan et al. 2019). Actually it is very difficult to interpret this radio emission as clear evidence for the PWN, since it might even be of a completely different nature, as already pointed out by Cigan et al. (2019). In any case the range of radio luminosities detected by ALMA can be used as a reliable upper limit for the PWN luminosity at 679 GHz, since a possible higher emission at this specific frequency should have been detected as well.

By moving the break frequency in the wide range of 10^{13}–10^{16} Hz and considering the limits imposed by Cigan's radio luminosities and available X-ray data, we obtain a range for the bolometric luminosity of the synchrotron spectrum of $\sim[0.15,\ 1.5] \times 10^{37}$ erg s^{-1}. The spectral energy distribution associated with a 679 GHz radio flux of exactly 2 mJy gives us a bolometric luminosity of 815 $L_\odot$, which is in agreement with the estimate of $\sim$850 $L_\odot$ discussed by Alp et al. (2018) when considering the multiwavelength upper limits for the flux and effects of the absorption along the line of sight.

This must then be converted into a range for the pulsar spin-down power. In order to do that, one has to assume a value for the conversion efficiency from rotational power into radiation (η). Unfortunately this parameter is poorly constrained, with some evidence for that of the Crab Nebula—believed to be one of the most efficient sources—to be $\eta \sim 30\%$ (Hester 2008). Here, in order to be as general as possible, we have considered a minimum conversion efficiency of $\eta = 5\%$ (which is very unlikely, meaning that almost all the energy is lost somewhere else) and a maximum one of $\eta = 70\%$. This translates into a wide range of possible pulsar spin-down luminosities: $\dot{E} \in [0.3,\ 30] \times 10^{37}$ erg s^{-1}. In Figure 3 we show how this range can be converted into a region of the pulsar's P–$\dot{P}$ diagram (the blue shaded area), making use of the relation $\dot{E} = 4\pi^2 I \dot{P}/P^3$, where $I \sim 10^{45}$ g cm^2 is the pulsar's momentum of inertia and $\dot{P}$ is the time derivative of its period. The region corresponding to a conversion efficiency of $\eta = 30\%$ is also shown (light blue). For a better comparison we report the position of the only three young systems known at present (with $t_{\rm age} \lesssim 1000$ yr), namely: the Crab Nebula, G21.5-0.9, and Kes75 (Gotthelf et al. 2000; Bietenholz & Bartel 2008; Hester 2008). Older sources cannot be consistently used to compare with this putative pulsar, since their long-term evolution has greatly changed their birth properties.

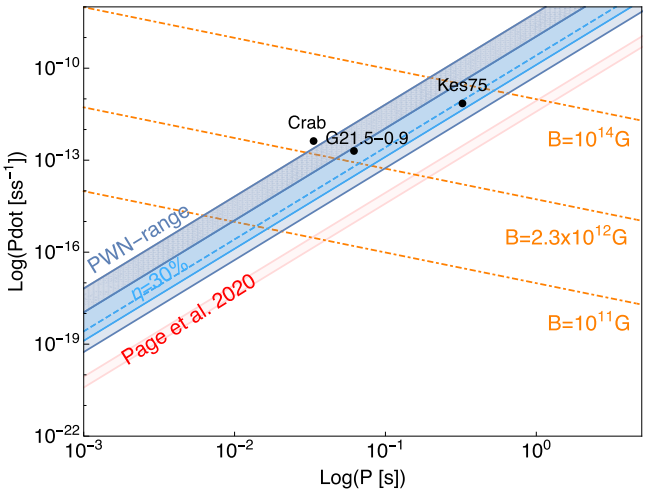

Figure 3. Position of the estimated range of possible spin-down luminosity of the putative pulsar in the P–$\dot{P}$ diagram (in blue; light blue shows that corresponding to a conversion efficiency $\eta = 30\%$). The cyan dashed line represents the case of a PWN having exactly a flux of 2 mJy at 679 GHz and a conversion efficiency $\eta = 30\%$. The upper part of the allowed region has been dashed with vertical lines to emphasize that it appears the most unlikely, both for the extremely low η it requires, as well as for a possible overinterpretation of the flux data in the estimate of the maximum blob luminosity. Orange dotted–dashed lines indicate a large range for magnetic fields associated with pulsars, plus the value computed as the average of the population of pulsars associated with X-ray PWNe (Kargaltsev & Pavlov 2008) (namely 2.3×10^{12} G). The range for the pulsar position as found in Page et al. (2020) is also reported for comparison as a red shaded area. The positions of three young pulsars associated with young PWNe (namely the Crab Nebula, G21.5-0.9, and Kes75) are shown with black dots.

It can be easily seen that the range we found for the pulsar position in the P–$\dot{P}$ diagram is perfectly consistent with that of known pulsars powering young systems. Moreover it must be noted that the apparent inconsistency with the range estimated in Page et al. (2020) (shown as the red shaded area in Figure 3) is due to the fact that the authors used the range of bolometric luminosities inferred from the measured flux at 679 GHz (L_R) to estimate the possible positioning of the pulsar in the P–$\dot{P}$ diagram (see Page et al. 2020, Figure 1), not considering that only a fraction of the spin-down power is converted into radiation (see, e.g., Bühler & Blandford 2014). Their range must then be considered as a lower limit for the spin-down luminosity: if the blob is illuminated by the pulsar—or if it is direct evidence for the emerging nebula—it is clear that the spin-down luminosity cannot be lower than the observed L_R.

Figure 3 shows as well the lines corresponding to a wide range of magnetic fields characteristic of the pulsar population (10^{11}–10^{14} G), using the relation $B = 3.2 \times 10^{19} (P\dot{P})^{1/2}$ G. The intermediate line shows the average magnetic field as computed from the known population of X-ray-emitting PWNe ($B \simeq 2.3 \times 10^{12}$ G, from Kargaltsev & Pavlov 2008). If the putative pulsar is characterized by a magnetic field close to the average value of pulsars associated with X-ray-emitting PWNe,

its period is expected to be in the range $P \in [30, 100]$ ms. If the conversion efficiency is similar to that usually assumed for the Crab (30%), this range reduces to $P \in [45, 80]$ ms.

3. Discussion

In this work, we have demonstrated that, at all epochs analyzed, the description of the broadband X-ray emission from SN 1987A requires a PL nonthermal component with absorption compatible with that of the cold and dense metal-rich ejecta in the innermost part of SN 1987A. The nonthermal nature of this high-energy source is supported by the temporal evolution of the 10–20 keV flux. In fact, the flux evolution of SN 1987A has been dramatically changing in the last two decades on a timescale of a few years or even months (see Figure 4 in A21 and references therein). In particular, the soft X-ray emission is currently fading away with time, while the hard one is still increasing, albeit at a slower rate. Both these trends are in stark contrast with the 10% flux variation in the 10–20 keV band. It is hard to explain how the thermal emission has changed significantly year by year in all other bands but has remained almost constant in the 10–20 keV band. On the other hand, the emission from a PWN is not expected to vary significantly on such a short timescale (much less than the pulsar spin-down age $\tau_0 \sim 1$ kyr).

The measured photon index $\Gamma \sim 2.8$ is compatible with the synchrotron emission from a PWN. DSA working at the outer shell of the remnant could also be invoked as a possible source of this radiation (see G21). We found that the addition of an unabsorbed PL to the $3kT$ model in fact improves the fit quality of the multiepoch observations. However, the best description of the spectra is achieved when heavy PL absorption is included, thus suggesting that the source of the nonthermal emission is located close to the center of the remnant, instead of the edge as needed in the DSA case. Furthermore, DSA requires a similar temporal evolution for radio and X-ray fluxes, while the flux in the 10–20 keV band has increased slightly (∼10%) between 2014 and 2020, and it is consistent with being constant at the 90% confidence level. In contrast, the flux in the radio band has increased by ∼60% (and, in general, has dramatically changed in all other bands) in the same time lapse (see Figure 4 in A21 and Cendes et al. 2018). In the light of these considerations we can exclude standard DSA as the mechanism producing the observed radiation, which we thus interpret as the result of nonthermal emission from a PWN located at the heart of SN 1987A.

We investigated the nature of the ∼10% variation observed in the best-fit 10–20 keV flux, making use of high-resolution MHD simulations of SN 1987A. In particular we exploited the MHD model B18.3 from Or20 and evaluated, in the time lapse analyzed, the variation of thermal flux arising from the shock-heated plasma in the 10–20 keV band and the decrease in the absorbing power of the innermost cold ejecta due to the expansion of the remnant. We found that both these effects concur, with similar weights, with the ∼10% increase in the flux in the 10–20 keV band, thus fitting nicely in the scenario of a PWN enshrouded by cold ejecta in the heart of SN 1987A. In particular, we found that the absorbed flux of the PL in correspondence with the Fe K emission line increases by a factor ∼5 between 2014 and 2020 (see first row in Figure 4), a clear signature of the decrease in the absorption of the expanding innermost ejecta.

To investigate also the possible thermal (blackbody) contribution of the NS embedded in the inner part of SN 1987A, we replaced the PL component with a blackbody (`bbodyrad` model in XSPEC). We found no improvements in the fit quality with respect to the $3kT$ model for a typical radius ($2\ \mathrm{km} < R < 20\ \mathrm{km}$) of the NS or CCO (De Luca 2008). Conversely, we found a significant improvement in χ^2 for temperature $kT_{\rm bb} \sim 4$ keV and with R of a few meters. However, the spectral shape of such an absorbed blackbody is practically indistinguishable from the absorbed PL, with all the radiation below ∼8 keV being suppressed by absorption by cold and dense ejecta. Given the unrealistically small radius found for the best-fit blackbody, we conclude that our X-ray spectra do not contain any hint of the NS radiation. Detailed analysis of the time evolution of the thermal X-ray emission from the NS will be discussed in a companion paper (A. Dohi et al. 2022, in preparation).

A21 stated that including a PL component leads to an unreasonably high abundance of Fe to reproduce the Fe K emission line. From the best-fit parameters in Table 2, it can be seen that by considering a PL emission absorbed by the innermost ejecta, the Fe abundance is fully consistent with the typical values found for the LMC, and with previous estimates (S21, A21). To further investigate the different plasma components contributing to the Fe K line, we produced synthetic XMM-Newton/pn spectra from model B18.3, separating the contributions from the three main plasma components of SN 1987A: the shocked material from the ring, that from the H II region, and the shocked ejecta (see Figure 4). We then included also the absorbed PL and summed all the contributions to generate the synthetic total spectrum (black data points in the first row of Figure 4). Finally, we compared the resulting spectrum with the observed one at each epoch (first row of Figure 4).

The observed Fe K flux can be correctly recovered by including the nonthermal component. The synthetic spectra in Figure 4 show how the different X-ray-emitting regions of SN 1987A contribute to the Fe emission at different epochs. While in 2012 the Fe K emission is mainly due to the shocked ring, especially to the lower-density material lying between the dense clumps, in 2020 the contribution of the ejecta to the emission line is as high as that of the ring. To better highlight this trend, we produced maps of continuum-subtracted line flux of the Fe K line from model B18.3, and compared them to the total distribution of emission measure (second, third, and fourth rows in Figure 4). The contours traced help to identify the origin of the Fe K flux. The contribution to Fe K flux from the shocked ejecta and shocked material from the H II region gradually increases from 2012 to 2020; this contribution is characterized by an average value of the ionization parameter significantly lower than that of the contribution due to the shocked material from the ring. For reference, a comparison with the hard thermal component reported by S21 for 2014 data is also shown. In the light of comparison between the MHD model and the observations, we suggest that, in the next few years, the main contribution to the Fe K line will come from the shocked ejecta lying in the outer envelope of SN 1987A.

4. Summary and Conclusions

In this paper we showed that the most likely and physically reasonable origin of the hard X-ray emission (>10 keV) observed with NuSTAR is nonthermal radiation emitted by a

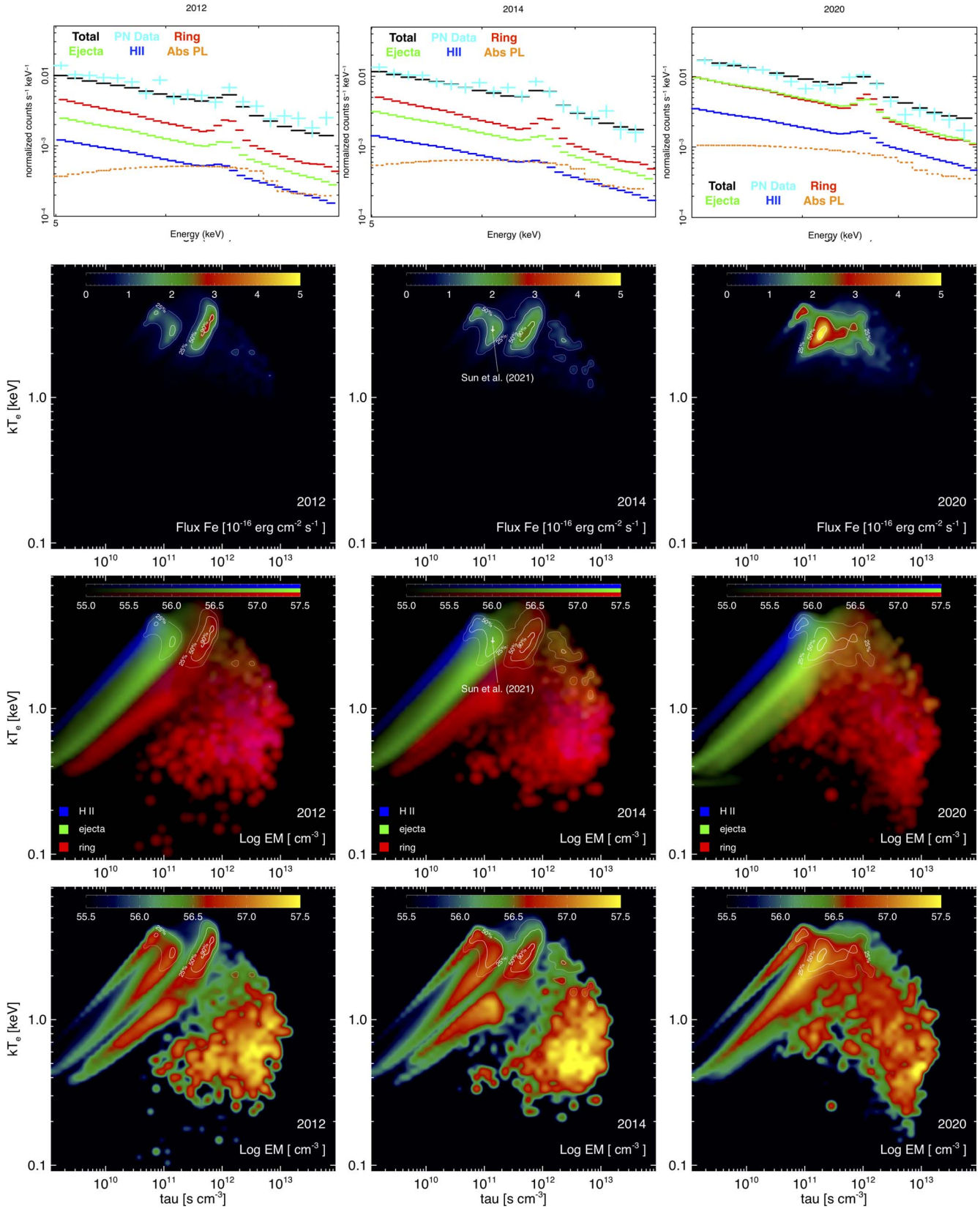

Figure 4. Comparison between Fe K observed emission lines and the various contributions estimated from the B18.3 model. From top to bottom: the first panel shows the synthetic spectra of the ring (red), ejecta (green), H II region (blue), absorbed PL (orange), the total synthetic spectrum (black), and the actual XMM-Newton/pn data (cyan); the second panel shows maps of the continuum-subtracted Fe K line flux; the third and fourth panels show maps of the distribution of emission measure for SN 1987A in logarithmic units, isolating the various components of the plasma and showing the total distribution, respectively. From left to right: the first column pertains to 2012, the second to 2014, and the third to 2020. White contours identify the regions where 25%, 50%, and 90% of Fe K originates. The panels relevant to 2014 also provide a comparison between the maps and the findings of S21 for the model with three thermal components.

heavily absorbed PWN embedded in the cold and dense ejecta of SN 1987A. Our findings can be summarized as follows.

1. The standard X-ray analysis of XMM-Newton, Chandra, and NuSTAR observations based on a purely thermal model shows significant residuals in the 10–20 keV band at all epochs. By including a power law, absorbed by the cold inner ejecta, these residuals disappear.
2. The best-fit nonthermal component is characterized by a photon index $\Gamma \sim 2.8$, which is compatible with being synchrotron emission. The spectral parameters of the absorbed power law are compatible with being constant at all epochs, indicating that this component is almost constant over a time lapse of eight years (2012–2020). An unabsorbed power law, representing the DSA scenario, provides a worse description of the spectra, indicating that the source of the nonthermal emission is embedded in the heart of SN 1987A. All the above lines of evidence favor a PWN rather than DSA as the origin of the flux excess above 10 keV.
3. The comparison of the observed spectra with those synthesized from a state-of-the-art MHD model of SN 1987A (Or20) shows again a significant flux excess in the 10–20 keV band. The MHD model describes only the thermal contribution to the emission. By adding the absorbed PL component, derived independently with the standard data analysis, to the synthetic spectra from the MHD model, the resulting spectra are compatible with the observed broadband X-ray spectra of SN 1987A at all epochs analyzed.
4. The 10–20 keV flux increases slightly by ∼10% in the time lapse analyzed. By exploiting the MHD model of SN 1987A, we found that this increase is entirely ascribable, with similar percentages, to the decrease in absorption by the cold and dense ejecta and to the increase in the thermal contamination in the high-energy band. In the same time lapse, the radio emission due to DSA in the outer shell of the remnant is observed to increase by ∼60% (Cendes et al. 2018). These lines of evidence exclude DSA as a possible mechanism powering the observed nonthermal emission.
5. The properties found for the X-ray nonthermal component and the upper limit on the radio luminosity of a putative PWN derived from ALMA's observations are fully compatible with a PWN spectrum described by a standard broken PL.
6. We derived the ranges of spin-down luminosity and period of the putative pulsar associated with the modeled synchrotron spectrum. We found values that are fully compatible with those inferred for other known young PWNe (as G21.5-0.9, and Kes75), thus leaving large room for the existence of a PWN inside SN 1987A.

This research has made use of the NuSTAR Data Analysis Software (NuSTARDAS) jointly developed by the ASI Space Science Data Center (SSDC, Italy) and the California Institute of Technology (Caltech, USA). This project has received funding from the European Union's Horizon 2020 research and innovation program under grant agreement No. 101004131 (SHARP). The MHD model was implemented with the PLUTO code developed at the Turin Astronomical Observatory (Italy) in collaboration with the Department of General Physics of Turin University (Italy) and the SCAI Department of CINECA (Italy). We acknowledge that the results of this research have been achieved using the PRACE Research Infrastructure resource Marconi based in Italy at CINECA (PRACE Award N.2016153460). Additional computations were carried out at the SCAN (Sistema di Calcolo per l'Astrofisica Numerica) facility for high performance computing at INAF–Osservatorio Astronomico di Palermo. E.G., M.M., S.O., B.O., F.B., and G.P. acknowledge financial contribution from the PRIN INAF 2019 grant "From massive stars to supernovae and supernova remnants: driving mass, energy and cosmic rays in our Galaxy" and the INAF mainstream program "Understanding particle acceleration in galactic sources in the CTA era." This work is supported by JSPS Grants-in-Aid for Scientific Research "KAKENHI" (A: grant No. JP19H00693; B: grant No. JP21K03545). S.N. and M.O. acknowledge supports from Pioneering Program of RIKEN for Evolution of Matter in the Universe (r-EMU) and RIKEN Interdisciplinary Theoretical and Mathematical Sciences Program (iTHEMS). S.N. also acknowledges the support from Pioneering Program of RIKEN for Evolution of Matter in the Universe (r-EMU). B.O. acknowledges Elena Amato, Niccolò Bucciantini, and Rino Bandiera for fruitful discussion.

Facilities: Chandra,[12] NuSTAR (Harrison et al. 2013), XMM-Newton (Jansen et al. 2001).

Software: CIAO (Fruscione et al. 2006), HEASOFT,[13] XSPEC (Arnaud 1996), NuSTARDAS[14] SAS (Gabriel et al. 2004), DS9,[15] PLUTO[16] (Mignone et al. 2012).

Appendix
PWN Emission in Soft X-Rays

The thermal emission from SN 1987A has been increasing with time in the last two decades. Therefore, the nonthermal emission, expected to be basically constant, should be easier to detect in the earlier epochs, when contamination by thermal emission was smaller. However, the absorption of the cold ejecta is significantly higher in the early stage of evolution of SN 1987A and it is not obvious to figure out which of the two effects (either reduced contamination by thermal emission or increased absorption) is the most relevant for the global emission. What we know is that no significant X-ray nonthermal emission has ever been detected in the band between 0.5 and 8 keV. Therefore, to test the scenario presented in this paper, we checked whether the PWN we detected is compatible with the Chandra observations performed before the launch of NuSTAR. In particular, we considered data collected by the Chandra/ACIS-S detector in 2003, 2014, and 2020 (see Table 1). We extracted spectra from the inner part of SN 1987A, the black circle of 0.″3 radius, focusing on the faintest region where the NS is expected to lie (black circle shown in upper panels of Figure 5). Since the inner area of SN 1987A is very faint, we combined the 2014 and 2020 spectra through the task `addascaspec` to decrease the width of the error bars.

The spectra were then optimally binned and compared with the emission from the PWN. We assumed a photon index $\Gamma = 2.8$ and norm $= 7.1 \times 10^{-4}$ photons s^{-1} keV^{-1} cm^{-2}, i.e., the PL parameters reported in Table 3. The PL component is

[12] https://cxc.harvard.edu/index.html
[13] https://heasarc.gsfc.nasa.gov/docs/software/heasoft/
[14] https://heasarc.gsfc.nasa.gov/docs/nustar/analysis/nustar_swguide.pdf
[15] https://sites.google.com/cfa.harvard.edu/saoimageds9/home?authuser=0
[16] http://plutocode.ph.unito.it

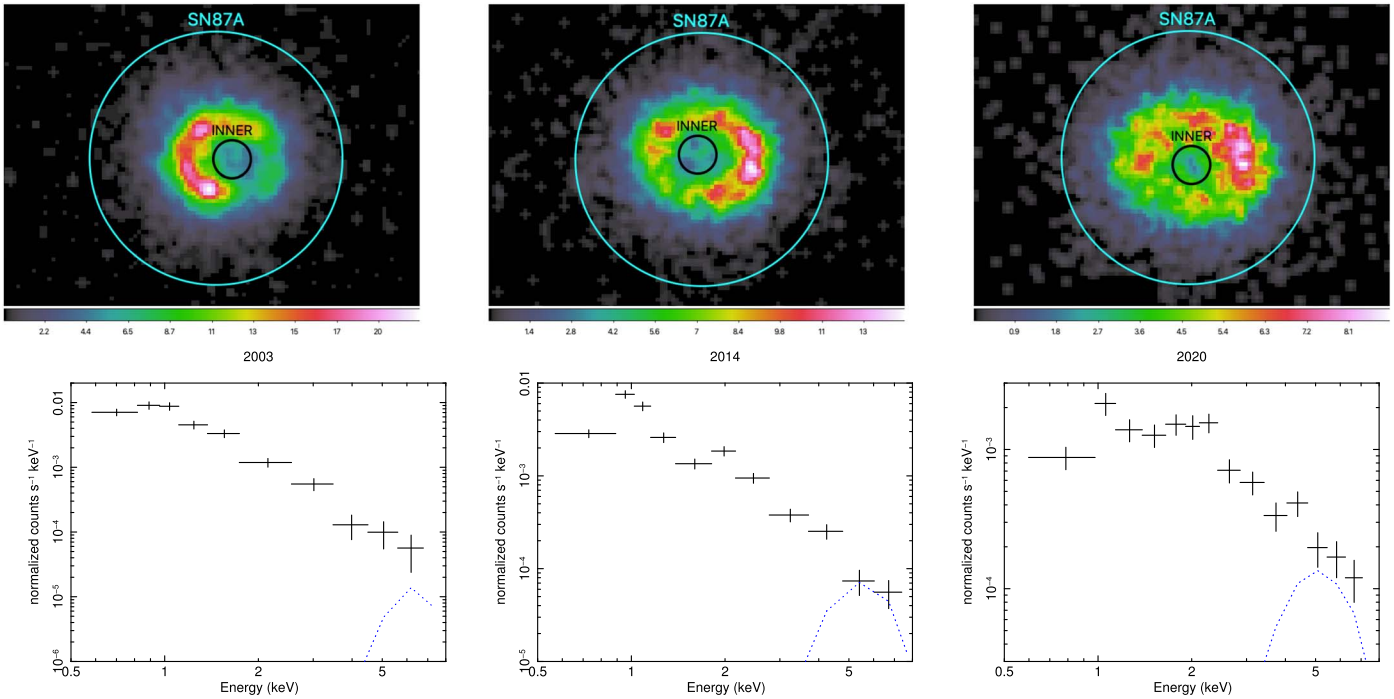

Figure 5. First row: Chandra/ACIS-S count images of SN 1987A in the 0.1–8 keV band in 2003 (left), 2014 (center), and 2020 (right). The images are smoothed with a Gaussian having a sigma of 1 pixel. The black and cyan circles mark the the inner faint region of SN 1987A, where the putative compact object is most likely lying, and the whole remnant. Second row: combined spectra of SN 1987A extracted from the Chandra observations performed in 2003 (left), 2014 (center), and 2020 (right). The black points represent the inner region and the blue curve shows the emission of the absorbed PL.

coupled to the proper `vphabs` component for the considered year, estimated from model B18.3. Since the inner faint part of SN 1987A is smaller than the Chandra/ACIS-S pixel size (0.″3 versus 0.″492), the observed flux must be corrected to take into account the effects of the point-spread function, particularly the encircled energy. Therefore, we included a multiplicative constant in the spectrum of the PWN when it is compared to the spectrum of the inner region. For a radius of 0.″3 and assuming the peak energy to be around 6 keV, this constant is ∼0.4 (https://cxc.harvard.edu/proposer/POG/pdf/MPOG.pdf). The resulting spectra for all the years are shown in the second row of Figure 5.

As is clear from the plots in Figure 5, in every year, the nonthermal emission is at least a factor ∼10 dimmer than the thermal emission up to 5 keV. At energies ∼5 keV, the absorbed PL reaches its peak but, in any case, it is below the observed spectrum.

Moreover, the emission observed in the inner area is due to the contamination of the shocked ring material, and the potential signal from the PWN would be mixed up with this contamination. At energies $\gtrsim$5 keV, the flux of the observed spectrum dramatically decreases and becomes compatible with the background. For all these reasons, the PWN is currently undetectable in the soft (0.5–8 keV) X-ray band.

ORCID iDs

Emanuele Greco https://orcid.org/0000-0001-5792-0690
Marco Miceli https://orcid.org/0000-0003-0876-8391
Salvatore Orlando https://orcid.org/0000-0003-2836-540X
Shigehiro Nagataki https://orcid.org/0000-0002-7025-284X
Lei Sun https://orcid.org/0000-0001-9671-905X
Jacco Vink https://orcid.org/0000-0002-4708-4219
Masaomi Ono https://orcid.org/0000-0002-0603-918X
Akira Dohi https://orcid.org/0000-0001-8726-5762
Giovanni Peres https://orcid.org/0000-0002-6033-8180

References

Alp, D., Larsson, J., Fransson, C., et al. 2018, ApJ, 864, 174
Alp, D., Larsson, J., & Fransson, C. 2021, ApJ, 916, 76
Arnaud, K. A. 1996, in ASP Conf. Ser. 101: Astronomical Data Analysis Software and Systems V, ed. G. H. Jacoby & J. Barnes (San Francisco, CA: ASP), 17
Bietenholz, M. F., & Bartel, N. 2008, MNRAS, 386, 1411
Bionta, R. M., Blewitt, G., Bratton, C. B., et al. 1987, PhRvL, 58, 1494
Borkowski, K. J., Blondin, J. M., & McCray, R. 1997, ApJ, 477, 281
Bühler, R., & Blandford, R. 2014, RPPh, 77, 066901
Cendes, Y., Gaensler, B. M., Ng, C. Y., et al. 2018, ApJ, 867, 65
Cigan, P., Matsuura, M., Gomez, H. L., et al. 2019, ApJ, 886, 51
De Luca, A. 2008, in AIP Conf. Proc. 983, 40 Years of Pulsars: Millisecond Pulsars, Magnetars and More, ed. C. Bassa et al. (Melville, NY: AIP), 311
Esposito, P., Rea, N., Lazzati, D., et al. 2018, ApJ, 857, 58
Frank, K. A., Zhekov, S. A., Park, S., et al. 2016, ApJ, 829, 40
Fransson, C., & Chevalier, R. A. 1987, ApJL, 322, L15
Fruscione, A., McDowell, J. C., Allen, G. E., et al. 2006, Proc. SPIE, 6270, 62701V
Gabriel, C., Denby, M., Fyfe, D. J., et al. 2004, in ASP Conf. Ser. 314, Astronomical Data Analysis Software and Systems (ADASS) XIII, ed. F. Ochsenbein, M. G. Allen, & D. Egret (San Francisco, CA: ASP), 759
Gaensler, B. M., & Slane, P. O. 2006, ARA&A, 44, 17
Gotthelf, E. V., Vasisht, G., Boylan-Kolchin, M., & Torii, K. 2000, ApJL, 542, L37
Greco, E., Miceli, M., Orlando, S., et al. 2021, ApJL, 908, L45
Haberl, F., Geppert, U., Aschenbach, B., & Hasinger, G. 2006, A&A, 460, 811
Harrison, F. A., Craig, W. W., Christensen, F. E., et al. 2013, ApJ, 770, 103
Hester, J. J. 2008, ARA&A, 46, 127
Jansen, F., Lumb, D., Altieri, B., et al. 2001, A&A, 365, L1
Kaastra, J. S., & Bleeker, J. A. M. 2016, A&A, 587, A151
Kargaltsev, O., & Pavlov, G. G. 2008, in AIP Conf. Proc. 983, 40 Years of Pulsars: Millisecond Pulsars, Magnetars and More, ed. C. Bassa et al. (Melville, NY: AIP), 171
Madsen, K. K., Harrison, F. A., Markwardt, C. B., et al. 2015, ApJS, 220, 8

Maggi, P., Haberl, F., Sturm, R., & Dewey, D. 2012, A&A, 548, L3
Maitra, C., Haberl, F., Sasaki, M., et al. 2022, A&A, 661, A30
McCray, R. 1993, ARA&A, 31, 175
McCray, R., & Fransson, C. 2016, ARA&A, 54, 19
Miceli, M., Orlando, S., Burrows, D. N., et al. 2019, NatAs, 3, 236
Mignone, A., Zanni, C., Tzeferacos, P., et al. 2012, ApJS, 198, 7
Ono, M., Nagataki, S., Ferrand, G., et al. 2020, ApJ, 888, 111
Orlando, S., Miceli, M., Pumo, M. L., & Bocchino, F. 2015, ApJ, 810, 168
Orlando, S., Ono, M., Nagataki, S., et al. 2020, A&A, 636, A22
Page, D., Beznogov, M. V., Garibay, I., et al. 2020, ApJ, 898, 125
Panagia, N. 1999, in IAU Symp. 190, New Views of the Magellanic Clouds, ed. Y. H. Chu et al. (Cambridge: Cambridge Univ. Press), 549
Park, S., Zhekov, S. A., Burrows, D. N., et al. 2006, ApJ, 646, 1001
Ravi, A. P., Park, S., Zhekov, S. A., et al. 2021, ApJ, 922, 140
Reynolds, S. P., Pavlov, G. G., Kargaltsev, O., et al. 2017, SSRv, 207, 175
Russell, S. C., & Dopita, M. A. 1992, ApJ, 384, 508
Slane, P. 2017, in Handbook of Supernovae, ed. A. W. Alsabti & P. Murdin (Berlin: Springer), 2159
Sugerman, B. E. K., Crotts, A. P. S., Kunkel, W. E., Heathcote, S. R., & Lawrence, S. S. 2005, ApJS, 159, 60
Sun, L., Vink, J., Chen, Y., et al. 2021, ApJ, 916, 41
Torres, D. F., Cillis, A., Martín, J., & de Oña Wilhelmi, E. 2014, JHEAp, 1, 31
Urushibata, T., Takahashi, K., Umeda, H., & Yoshida, T. 2018, MNRAS, 473, L101
Vissani, F. 2015, JPhG, 42, 013001
West, R. M., Lauberts, A., Jorgensen, H. E., & Schuster, H. E. 1987, A&A, 177, L1
Wilms, J., Allen, A., & McCray, R. 2000, ApJ, 542, 914
Zhekov, S. A., McCray, R., Dewey, D., et al. 2009, ApJ, 692, 1190